Bootstrap Dual-Polarimetric Spectral Density Estimator

Arturo Y. Umeyama, *Student Member, IEEE*, Sebastián M. Torres, *Senior Member, IEEE*, and Boon Leng Cheong

***Abstract*— Weather radar variables provide useful information about the characteristics and motion of hydrometeors. However, the bulk information may be masked, when the meteorological signal of interest is contaminated by clutter. The dual-polarimetric spectral densities (DPSDs) may unveil additional information about the polarimetric characteristics of the groups of scatterers moving at different Doppler velocities in a given radar resolution volume. Previous DPSD estimation methods required averaging a large number of spectra (obtained from different spatial locations or times), or averaging in frequency to get accurate estimates; though by doing so, the resolution is degraded, and the important features of the meteorological phenomenon may be masked. In an attempt to overcome these limitations, the Bootstrap DPSD estimator is proposed, which allows the estimation of DPSDs from a single dwell with minimal spatial, temporal, or spectral resolution loss. The performance and the limitations of the Bootstrap and conventional DPSD estimators are assessed when identifying signals with different polarimetric signatures of scatterers moving at different radial velocities in the radar volume. The advantages of the Bootstrap DPSD estimator as a tool for the polarimetric spectral analysis are demonstrated with a few examples of polarimetric spectral signatures in data from tornado cases. It is expected that, with the Bootstrap DPSD and the polarimetric spectral analysis, it will be possible to better understand tornado dynamics and their connection to weather radar measurements, as well as to elucidate important scientific questions that motivated this paper.**

***Index Terms*— Bootstrap, polarimetric spectral density, spectral estimation, weather radar.**

I. Introduction

IT IS known that the tornadoes are one of the greatest weather-related threats to life and property in the U.S. Violent winds and airborne debris in tornadoes are responsible for injuries and fatalities [1], and can also inflict major structural damage [2] exceeding billions of dollars in costs [3]. More knowledge about tornadoes would make possible the mitigation of such devastating consequences. However, tornado mechanics are still not completely understood [4]. Weather radars are essential in tornado studies, since they allow the retrieval of information in a way that would otherwise be extremely difficult and dangerous [5]. Moreover, with polarimetric radars, more accurate discrimination of meteorological and nonmeteorological scatterers within the radar resolution volume is possible [6]. Since the polarimetric signatures of debris lofted by tornadoes depend on their electrical size, shape, orientation, and concentration [7], they can be noticeably different from those of hydrometeors and can be used for enhanced tornado detection [8]. These tornadic debris signatures (TDSs) are tornado-scale polarimetric signatures with distinctive characteristics collocated with a tornado vortex, visible in radar observations after a tornado is lofting debris to the level of the radar beam [9], and are related to the ejection and centrifuging of hydrometeors and debris by the cyclone [10]. Additionally, they are the clear indicators of tornadoes, when ground observation is limited or impossible (e.g., at night or during heavy rainfall) [11].

In the recent years, TDSs have been used in different applications, e.g., improving the warning decision-making process, assessing a potential tornado threat [12], [13], enhancing the confidence of tornado detection [14], and assessing tornado damage potential and intensity [15]. Several studies [8], [16], [17] have shown the evidence of negative differential reflectivity (Z_{DR}) values in TDS from different tornado cases, suggesting a possible common alignment of the debris within the tornadic vortex, or a scattering in the Mie regime due to large debris. However, it is still unknown exactly how the characteristics of different debris types affect the different polarimetric variables. Furthermore, centrifuging effects cause hydrometeors and debris to move at slightly different velocities within a tornado vortex, and since Doppler radars measure the motion of the scatterers rather than the actual wind speed, significant biases can be introduced in the wind radar measurements [10]. This is especially true for the TDS, where the debris is the dominant scatterers in the radar resolution volume [8]. Hypothetically, this error in measurement could be corrected if the velocity of the debris was known and could be separated from the velocity of hydrometeors, which passively trace the wind. Since the radar variables are computed by averaging the contribution of all scatterers within a radar resolution volume, an alternative way to retrieve the velocities must be employed, which can be achieved through the spectral analysis.

Manuscript received September 9, 2016; revised November 8, 2016; accepted December 13, 2016. Date of publication January 16, 2017; date of current version February 24, 2017. This work was supported by the National Science Foundation under Grant AGS-1303685.

A. Y. Umeyama is with the Advanced Radar Research Center and the School of Electrical and Computer Engineering, The University of Oklahoma, Norman, OK 73019 USA (e-mail: aumeyama@ou.edu).

S. M. Torres is with the Cooperative Institute for Mesoscale Meteorological Studies, the School of Electrical and Computer Engineering, also with the Advanced Radar Research Center, The University of Oklahoma, Norman, OK 73072 USA, and also with the National Oceanic and Atmospheric Administration/Office of Oceanic and Atmospheric Research National Severe Storms Laboratory, Norman, OK 73072 USA.

B. L. Cheong is with the Advanced Radar Research Center, The University of Oklahoma, Norman, OK 73019 USA.

Color versions of one or more of the figures in this paper are available online at http://ieeexplore.ieee.org.

Digital Object Identifier 10.1109/TGRS.2016.2641385

The power spectral density (PSD) of weather radar signals is the power-weighted distribution of the radial velocities of the scatterers in a radar resolution volume [18]. Reference [19] found that approximately 75% of the spectra observed with a radar from precipitation at close ranges were Gaussian. For the other 25% of the cases with non-Gaussian spectra, the spectral analysis can provide important information about the distribution of radial velocities in the radar resolution volume, and it was found in [20] that many tornado spectra exhibit non-Gaussian distributions of Doppler velocities. Moreover, in the cases with more than one signal, e.g., a weather signal with nonzero mean radial velocity mixed with ground clutter, the spectra will show the distribution of both signals as a function of Doppler velocity with peaks corresponding to each type of scatterer, where the spectrum of the ground clutter signal is centered about zero and the spectrum of the weather signal can occupy any Doppler-velocity band [18]. Provided that the weather signal does not have a near-zero mean radial velocity and a narrow spectrum width, and the ground clutter can be filtered from the spectrum without significantly corrupting the weather signal [21]. In the cases where the signals overlap in the spectrum, techniques have been developed to mitigate the clutter influence and reconstruct the weather signal to provide better radar estimates [22], [23]. However, it is difficult to discriminate the nature of the nonstatic scatterers contained in the spectrum, since the peaks in a PSD do not contain any information other than the power returns and their radial velocity.

Additional spectral information can be gathered from the dual-polarimetric spectral densities (DPSDs) [24]. The DPSD depicts the polarimetric characteristics of scatterers moving at different Doppler velocities within a radar resolution volume. These tools for the polarimetric spectral analysis provide three additional spectral variables: the spectral differential reflectivity (sZ_{DR}), the spectral correlation coefficient ($s\rho_{\mathrm{HV}}$), and the spectral differential phase ($s\phi_{\mathrm{DP}}$). It is hypothesized that the discrimination of scatterer groups would be possible by correlating the DPSD values of unknown scatterers to those corresponding to different scatterer types with known polarimetric characteristics.

Previous works involving DPSDs have employed different methods for their estimation in different applications. Some works [24]–[26] have dealt with the spectral classification of scatterers to identify nonmeteorological targets, using range-averaged DPSDs. In [27], improved measurements of atmospheric returns were found using scan-to-scan-averaged DPSDs. Others [28]–[33] studied the microphysics and dynamics of different weather events using DPSDs estimated by averaging different scans and independent simulated spectra. Additionally, [34] studied the statistical quality of the spectral polarimetric variables, showing that 20 independent observations are needed to ensure optimal quality.

The main constraint in achieving desirable error levels to perform polarimetric spectral analyses for tornado observations is the limited amount of independent observations available. Multiple-dwell DPSD estimates account for this limitation by averaging spectra from adjacent azimuthal or radial locations and different scans, or even by smoothing the spectral estimates, but they ultimately end up reducing the spatial, temporal, and/or spectral resolution. Since tornadoes are events that evolve rapidly in time, in a relatively small spatial extent and with different scatterers contained within the tornadic vortex [15], it is critical to preserve the best resolution possible in all dimensions, thus the methods in the previous literature are not well suited.

In this paper, the Bootstrap DPSD estimator is presented, which accounts for the aforementioned limitations and computes the DPSD using only one dwell and resulting in minimal resolution loss. In Section II, several methods to estimate the spectral variables are presented, and an assessment of the advantages and limitations of the DPSD estimation methods is included. A description of the key aspects and considerations taken in the design of the Bootstrap DPSD estimator is presented in Section III. Thorough analyses of the performance of the Bootstrap DPSD estimator under different scenarios are presented in Section IV. Section V shows the results of using the Bootstrap DPSD estimator on data sets of a real weather event. Finally, concluding remarks and recommendations for the future work are presented in Section VI.

II. Spectral Estimation Methods

A. PSD Estimators

For PSD estimation, there are nonparametric and parametric methods. The former type makes no assumptions about the structure of the underlying phenomena, while the latter assumes that their structure can be modeled. Because the atmosphere is constantly changing, it is extremely difficult to parameterize a model for each case. Therefore, nonparametric methods are better suited for this paper.

1) Periodogram: One of the most common nonparametric methods to compute the PSD is the periodogram because of its relative simplicity and low computational cost. This method consists in applying the discrete Fourier transform (DFT) to the windowed I/Q time-series signal to obtain

$$Z_{\mathrm{H,V}}(k) = \sum_{m=0}^{M-1} d(m) V_{\mathrm{H,V}}(m) e^{-j2\pi mk/M} \qquad (1)$$

where the signal $V_{\mathrm{H,V}}(m)$ corresponds to either the horizontal (H) or vertical (V) channel, and $d(m)$ is the power-normalized data windowing function used to contain spectral leakage [35]. Then, the estimates of the H-, V-, and cross-spectrum PSDs can be obtained as

$$s\hat{S}_{\mathrm{H,V}}(k) = \frac{|Z_{\mathrm{H,V}}(k)|^2}{M} \qquad (2)$$

and

$$s\hat{S}_{\mathrm{X}}(k) = \frac{Z_{\mathrm{H}}(k) Z_{\mathrm{V}}^{*}(k)}{M} \qquad (3)$$

where M is the total number of samples in the dwell and k is the spectral index ($0 \leq k < M$). In spite of its advantages, the periodogram comes with limitations regarding the accuracy and precision of the PSD estimates. Many variants of the periodogram have been proposed in the literature to address these issues, some of which are described next.

2) Welch's Method: The method proposed by Welch [36] consists in dividing the time series into overlapping segments. The PSD of each segment is computed with the periodogram, and these partial estimates are then averaged to reduce the variance of the spectral estimates [37]. The PSD estimate of a single dwell with Welch's method is obtained as follows:

$$Z_i(k) = \sum_{m=0}^{L-1} d(m)V[m + i(L-O)]e^{-j2\pi mk/L} \quad (4)$$

$$s\hat{S}_i(k) = \frac{|Z_i(k)|^2}{L} \quad (5)$$

$$s\hat{S}(k) = \frac{1}{Q}\sum_{i=0}^{Q-1} s\hat{S}_i(k) \quad (6)$$

for $m = 0, \ldots, L-1$; $k = 0, \ldots, L-1$; and $i = 0, \ldots, Q-1$, where $Q = \lfloor \frac{M-O}{L-O} \rfloor$ is the number of segments, O is the amount of segment overlap, L is the segment length, and $\lfloor\cdot\rfloor$ is the floor function. Here, the H, V, or X subscripts for the PSDs have been omitted for simplicity, but it is important to note that the general procedure is similar to (2) and (3).

Welch's method produces smoother estimates, because the PSDs of different segments are averaged. However, since it reduces the number of samples to compute the partial PSD estimates, the spectral resolution is degraded significantly, although the variance is also reduced by a factor of Q (without overlap). Furthermore, by allowing the overlap of the time-series signal segments, the partial PSD estimates are no longer independent even though the tapered windowing function helps to decorrelate these estimates.

3) Daniell's Method: The smoothed periodogram method proposed by Daniell [38] reduces the variance of the estimate in a different manner than with the methods described above. In this method, a moving-average filter is applied to the "raw" periodogram estimate [37]. To obtain the PSD estimate with Daniell's method, we first get an estimate using (1)–(3). Then, a moving-average filter is applied as

$$s\hat{S}_{\mathrm{H,V,X}}(k) = \frac{1}{2p+1}\sum_{k'=\langle k-p\rangle_M}^{\langle k+p\rangle_M} s\hat{S}_{\mathrm{H,V,X}}(k') \quad (7)$$

where $2p+1$ is the length of the filter, and $\langle\cdot\rangle_M$ is the modulo M operator. Clearly, this method trades spectral resolution for the reduction of variance, and it may lead to higher bias as it smoothes the raw PSD. Additionally, when the spectral components of the signals of interest are too close, the ability to resolve them individually may be lost due to this smearing effect.

B. DPSD Estimators

Estimates of the spectral polarimetric variables are obtained in a similar way to the polarimetric radar variables, but using the PSDs instead. The spectral differential reflectivity and the spectral correlation coefficient can be obtained as

$$s\hat{Z}_{\mathrm{DR}}(k) = \frac{\sum_{i=1}^{K} s\hat{S}_{\mathrm{H}}^{(i)}(k)}{\sum_{i=1}^{K} s\hat{S}_{\mathrm{V}}^{(i)}(k)} \quad (8)$$

and

$$s\hat{\rho}_{\mathrm{HV}}(k) = \frac{\left|\sum_{i=1}^{K} s\hat{S}_{\mathrm{X}}^{(i)}(k)\right|}{\sqrt{\sum_{i=1}^{K} s\hat{S}_{\mathrm{H}}^{(i)}(k)\sum_{i=1}^{K} s\hat{S}_{\mathrm{V}}^{(i)}(k)}} \quad (9)$$

where K is the number of independent spectra that are averaged to obtain useful DPSD estimates. In this paper, the spectral differential phase will not be included, because it does not convey as much information to discriminate hydrometeors from debris.

Operational weather radars perform a scan every few minutes, which yield one independent spectrum ($K = 1$) for each radar resolution volume. Using the periodogram estimator, for the spectral differential reflectivity, the spectral components of the PSD have significantly large variance, providing a poor sZ_{DR} estimate. Additionally, it can be shown that the spectral correlation coefficient estimate fails to produce any useful results. By combining (2), (3), and (9), for $K = 1$

$$\begin{aligned} s\hat{\rho}_{\mathrm{HV}}(k) &= \frac{|s\hat{S}_{\mathrm{X}}(k)|}{\sqrt{s\hat{S}_{\mathrm{H}}(k)s\hat{S}_{\mathrm{V}}(k)}} = \frac{|Z_{\mathrm{H}}(k)Z_{\mathrm{V}}^{*}(k)|}{\sqrt{|Z_{\mathrm{H}}(k)|^2|Z_{\mathrm{V}}(k)|^2}} \\ &= \frac{|Z_{\mathrm{H}}(k)||Z_{\mathrm{V}}^{*}(k)|}{|Z_{\mathrm{H}}(k)||Z_{\mathrm{V}}(k)|} = 1 \end{aligned} \quad (10)$$

which shows how the $s\rho_{\mathrm{HV}}$ estimate always equals 1. This limitation can be overcome in different ways: either by using PSD estimators that perform averaging (single-dwell estimates), or by averaging PSDs from different sources, such as adjacent radar resolution volumes in azimuth, range, or consecutive scans.

1) Single-Dwell Estimators: Some of the PSD estimation methods described in Section II.A can provide DPSD estimates using data from a single dwell by reducing the statistical errors through averaging in the frequency domain. To summarize the PSD estimation methods, the periodogram estimates have the best frequency resolution but no averaging of PSDs is performed, and thus, it yields DPSD estimates with high bias and variance. The Welch estimator averages the PSDs of multiple segments with a variable frequency resolution that is, at best, worse than that obtained with the periodogram. The Daniell estimator averages multiple spectral coefficients and may consequently affect the ability to resolve closely spaced spectral components. Albeit useful in cases where no other type of averaging can be performed, these methods degrade the frequency resolution (Welch) or add additional spectral "smearing" (Daniell).

2) Multiple-Dwell Estimators: As previously mentioned, DPSDs can also be estimated by averaging PSDs from different sources, such as adjacent radar resolution volumes in azimuth, range, or consecutive scans. The impact of averaging in a particular dimension is assessed next.

a) Range averaging: More spectra may be acquired from spatially correlated radar resolution volumes [24]–[26]. If the range locations of a particular ray are chosen to be averaged, the range resolution is degraded by at least a factor of two. Depending on the range resolution of the radar, this could be quite significant as important spatial features of the weather phenomenon may be masked by averaging. On the other hand, since the range dimension of the resolution volume remains constant while the resolution volume increases in size with range due to the antenna beamwidth, and since range may be oversampled, range averaging may be a less compromising option in regard to resolution loss.

b) Azimuth averaging: A different spatial averaging can be performed using independent spectra from adjacent radar resolution volumes in azimuth. Similar to range averaging, the azimuthal resolution is degraded at least by a factor of two. At farther ranges, the radar resolution volume gets wider in azimuth resulting in degraded spatial resolution, while for a constant range, the resolution volumes will be similar in size. Thus, averaging in azimuth may be favored over range averaging at closer ranges. Additionally, if the azimuth is oversampled or if signal processing techniques, such as the superresolution [39], are used, the tradeoffs of azimuth averaging may be acceptable.

c) Scan-to-scan averaging: Averaging spectra from consecutive scans can also be performed to obtain better DPSD estimates, provided the spectra are somewhat correlated in time (i.e., slow moving phenomena or short scan times) [27]–[30]. By doing so, it must be ensured that the observations are based on the same location in space for a given event. However, to correctly capture the evolution of certain weather events, such as tornadoes, the time between consecutive scans for a given radar resolution volume must be considerably short [40], [41].

III. Bootstrap DPSD Estimator

As mentioned before, the quality of the DPSD estimates is limited by the number of available independent observations. The methods presented in Section II.B yield the estimates of sufficient quality provided that the number of independent measurements is large (larger than about 20). However, good temporal and spatial resolutions are required to capture the important features of tornadic storms, as well as a good spectral resolution to discriminate the velocities of hydrometeors and debris. For these reasons, it may be extremely difficult in practice to obtain the required number of measurements and to satisfy these constraints with currently available techniques for DPSD estimation. The Bootstrap DPSD estimator is presented in this paper as an alternative method that overcomes some of the limitations of the conventional PSD and DPSD estimators.

It is well known that the bootstrap is a statistical method, which consists of the random resampling with the replacement of the observed data [42]–[46]. Briefly, the Bootstrap DPSD estimator is the result of combining the bootstrap method with the DPSD estimator using averaged periodogram PSD estimates. The basic idea is to generate bootstrapped *pseudorealizations* of the weather radar I/Q time-series signals, in order to construct a bootstrap aggregate of the PSD estimated from the I/Q pseudorealizations from which a DPSD estimate can be obtained. The signals of the H and V channels are bootstrapped as a pair in order to preserve the cross correlation between channels. Since the processes controlling the I/Q time-series signals are correlated, the signals must be conditioned prior to the generation of bootstrapped pseudorealizations, such that additional information can be extracted from each signal without destroying the spectral information and/or degrading the quality of the estimates. A block bootstrap method [47] is employed to generate a suitable number of pseudorealizations from which the PSDs are computed.. These are then averaged to obtain a DPSD estimate. Finally, a bias correction technique is applied to obtain the Bootstrap DPSD estimate. A block diagram of the conventional and Bootstrap DPSD estimators is shown in Fig. 1. The algorithm of the Bootstrap DPSD estimator is described next.

A. Algorithm Description

1) Construct the Extended Time-Series Signal $X_{H,V}(m)$: The purpose of an extended signal is to provide added variability (for bootstrapping) while keeping the spectral characteristics as close as possible to those of the original signal through coherency corrections. To construct it, begin by concatenating three instances of the signal $\mathbf{V}$. Since this periodic extension adds discontinuities that reduce the coherency of the signal, corrections must be applied. That is, the left extension is backward corrected and the right extension is forward corrected as

$$\mathbf{X}_{\mathrm{H,V}} = \{\mathbf{V}^{\mathrm{L}}_{\mathrm{H,V}}, \mathbf{V}_{\mathrm{H,V}}, \mathbf{V}^{\mathrm{R}}_{\mathrm{H,V}}\} \tag{11}$$

where

$$\mathbf{V}^{\mathrm{L}}_{\mathrm{H,V}} = C^{-}_{\mathrm{X}}\{V_{\mathrm{H,V}}(0), \ldots, V_{\mathrm{H,V}}(M-2)\} \tag{12}$$

$$\mathbf{V}^{\mathrm{R}}_{\mathrm{H,V}} = C^{+}_{\mathrm{X}}\{V_{\mathrm{H,V}}(1), \ldots, V_{\mathrm{H,V}}(M-1)\} \tag{13}$$

and the correction factors $C^{-}_{\mathrm{H,V}}$ and $C^{+}_{\mathrm{H,V}}$ can be obtained as

$$C^{+}_{\mathrm{X}} = \frac{1}{2}\left[\frac{V_{\mathrm{H}}(M-1)}{V_{\mathrm{H}}(0)} + \frac{V_{\mathrm{V}}(M-1)}{V_{\mathrm{V}}(0)}\right] \tag{14}$$

and

$$C^{-}_{\mathrm{X}} = \frac{1}{2}\left[\frac{V_{\mathrm{H}}(0)}{V_{\mathrm{H}}(M-1)} + \frac{V_{\mathrm{V}}(0)}{V_{\mathrm{V}}(M-1)}\right]. \tag{15}$$

In the design of the coherency correction factors, the tradeoffs of a few different schemes were studied [48]. The selected correction factor was empirically found to have the best error performance for different simulation parameters. Two important design criteria that determined the selection of these correction factors were the small amount of incoherency added to the signal (reflected in the bias of $s\hat{\rho}_{\mathrm{HV}}$) and the robustness in cases where the signals have differential phase of approximately $\pm 180°$. It should also be noted that the extensions are of length $M-1$ due to the fact that, with the correction, the first (or last) element of a block is "matched" to the last (or first) element of the adjacent block (i.e., there is a duplicate sample on each extension of the signal). The length of the extended signal then becomes $M' = 3M-2$, from which the $2M-1$ blocks of length M can be drawn as bootstrap samples. A pseudorealization obtained by resampling from this set of blocks is still prone to spectral leakage, albeit lesser than in the case where no coherency correction is applied.

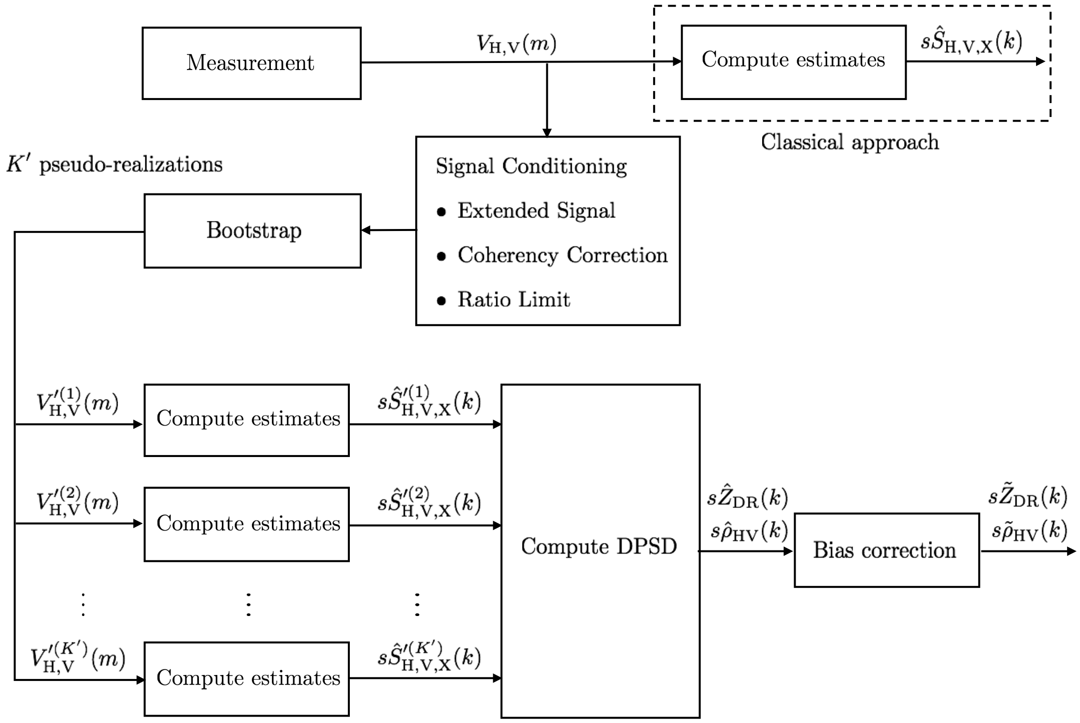

Fig. 1. Block diagram of the conventional and Bootstrap DPSD estimators.

2) Compute the Maximum Ratio of Corrected Samples r_{max}: The second step attempts to further improve the quality of the bootstrapped estimates with a careful selection of the blocks. Pseudorealizations with more discontinuities (corrected or not) are more likely to exhibit more spectral leakages due to the loss of coherency. Hence, instead of using all the blocks of the extended signal, it is possible to select the set of blocks that contain more original samples than corrected samples. The concept of the ratio of corrected samples in a block (or pseudorealization) is introduced as

$$r = \frac{M_{\mathrm{corrected}}}{M} \tag{16}$$

where $M_{\mathrm{corrected}}$ is the number of corrected samples in the block. In this sense, the original sequence has a ratio $r = 0$, while blocks beginning at samples $M/2$ and $3M/2$ have a ratio close to $r = 0.5$, and blocks beginning at samples 1 and $2M - 1$ have a ratio close to $r = 1$. For example, by establishing a threshold for blocks that have a maximum ratio of $r = 0.5$, it can be guaranteed that all the blocks in the reduced population will have at least 50% of the original samples. Clearly, this strategy can additionally reduce the spectral leakage by mitigating the incoherencies remaining in the periodic extension of the original signal at the price of reducing the number of permissible pseudorealizations. The spectral leakage is reduced with this strategy mainly because the data points near the discontinuities are deemphasized by the window tails while more weight is placed on the original samples. This is equivalent to applying a sliding data window on a signal while allowing the signal to be periodically extended. The ratio that maximizes the amount of information depends on the data windowing function used in the analysis. A good compromise between spectral leakage and statistical errors is obtained by limiting the selection to blocks with a maximum ratio of

$$r_{\max} = \frac{1 - \sqrt{\frac{1}{M}\sum_{m=0}^{M-1}\left|\frac{d(m)}{\max d(m)}\right|^2}}{2} = \frac{1-\sqrt{\alpha}}{2} \tag{17}$$

where α is the mean power of the data windowing function, and the amplitude $\sqrt{\alpha}/2$ is related to the number of points in the data window that contributes the most to the spectral estimate. With this definition, r is bounded between 0.5, where half of the samples are corrected, and 0, where none of the samples are corrected. It can be easily seen that more tapered windows lead to higher maximum ratio and vice versa. In other words, the amplitude of the data windowing function determines the number of corrected samples, as weighted by the window, that can be present on either end of a sequence before the spectral leakage becomes significant.

3) Bootstrap the Extended Signal: For the third step, the conditioned signal is bootstrapped and a number of pseudorealizations are generated. The moving block bootstrap [49], [50] is a dependent data bootstrap method that consists of dividing the signal into overlapping blocks that are resampled with replacement with equal probability. An implementation on weather radar I/Q time-series signal is as follows. Let the set of available blocks (with maximum ratio $r_{\max}$) for resampling from the extended signal be defined as

$$\mathcal{B} = \{\mathbf{B}_0, \mathbf{B}_1, \ldots, \mathbf{B}_{N'-1}\} \tag{18}$$

where each block of length M is given by

$$\mathbf{B}_j = \{X_{\mathrm{H,V}}(j), \ldots, X_{\mathrm{H,V}}(j+M-1)\} \tag{19}$$

for $0 \le j \le N'-1$, where $N' = \lfloor 2r_{\max}(M-1)+1 \rfloor$ is the number of available blocks. An I/Q pseudorealization $\mathbf{V}'^{(i)}_{\mathrm{H,V}}$ is obtained as

$$\mathbf{V}'^{(i)}_{\mathrm{H,V}} = \mathbf{B}_{j^{(i)}} \tag{20}$$

for $0 \le i \le K'-1$, where K' is the number of pseudorealizations to be generated and $j^{(i)}$ is a uniformly distributed random integer in the interval $[0, N'-1]$. In other words, the K' blocks of length M are drawn from the ratio-limited extended signal.

An additional step is taken to correct the power of the I/Q pseudorealizations. Since the coherency correction factors scale both the magnitude and phase of corrected samples, a power correction must be applied to preserve the power of the original signal. Let $\hat{P}_{\mathrm{H,V}}$ be the estimated average power of the H and V channels of the original signal, and $\hat{P}'_{\mathrm{H,V}}$ be the average power of the H and V channels of a pseudorealization. The average power of each pseudorealization is matched to the average power of the original signal; mathematically

$$V''_{\mathrm{H,V}}(m) = \sqrt{\frac{\hat{P}_{\mathrm{H,V}}}{\hat{P}'_{\mathrm{H,V}}}}\, V'_{\mathrm{H,V}}(m), \quad 0 \le m < M \tag{21}$$

so that

$$\hat{P}''_{\mathrm{H,V}} = \hat{P}_{\mathrm{H,V}} \tag{22}$$

and the power of the original signal is preserved.

4) Compute the DPSDs: The next step of the algorithm involves computing M-sample periodogram PSDs of the pseudorealizations with (1)–(3), and averaging them to compute the DPSDs with (8) and (9) (also with M spectral components).

5) Apply Bias Correction to DPSDs: The final step involves correcting the DPSD estimates for inherent biases. In general, the expected value of the DPSD estimate and the true value are related by

$$E[s\hat{Z}_{\mathrm{dr}}(k)] = sZ_{\mathrm{dr}}(k) + \mathrm{bias}[s\hat{Z}_{\mathrm{dr}}](k) \tag{23}$$

and

$$E[s\hat{\rho}_{\mathrm{HV}}(k)] = s\rho_{\mathrm{HV}}(k) + \mathrm{bias}[s\hat{\rho}_{\mathrm{HV}}](k) \tag{24}$$

where sZ_{dr} is the spectral differential reflectivity expressed in linear units (in decibel units and $sZ_{\mathrm{DR}} = 10\log sZ_{\mathrm{dr}}$). The analytical expressions of the statistical errors of $s\hat{Z}_{\mathrm{DR}}$ and $s\hat{\rho}_{\mathrm{HV}}$ were determined in [34]. The biases of the DPSD depend on the number of independent spectra K, the spectral SNR of the H and V channels, $s\mathrm{SNR}_{\mathrm{H,V}}$, and the true spectral correlation coefficient, $s\rho_{\mathrm{HV}}$. The bias expressions derived from [34] are

$$\frac{\mathrm{bias}[s\hat{Z}_{\mathrm{dr}}](k)}{s\hat{Z}_{\mathrm{dr}}(k)} = \frac{1}{\beta K}\left[1 - s\hat{\rho}^2_{\mathrm{HV}}(k)\right] \tag{25}$$

and

$$\frac{\mathrm{bias}[s\hat{\rho}_{\mathrm{HV}}](k)}{s\hat{\rho}_{\mathrm{HV}}(k)} = \frac{1}{\beta K}\left\{\frac{[1 - s\hat{\rho}^2_{\mathrm{HV}}(k)]^2}{4s\hat{\rho}^2_{\mathrm{HV}}(k)}\right\}. \tag{26}$$

The sSNR terms are neglected, because it is assumed that the SNR of the signal of interest is high (more than 20 dB). β is a factor that compensates for the fact that the bootstrapped pseudorealizations are not independent, and it adjusts the estimated DPSD such that the error between the DPSD estimate and the true value is minimized. Given the complexity in deriving an analytical expression for bootstrapped time series with arbitrary distributions, β was determined empirically by fitting the different values of r such that the error was minimized for all K. The result is

$$\beta = \begin{cases} (1-r)^{-3.3} - 2(1-r)^{1.1}, & \text{for } K = 1 \\ (1-r)^{-4.5} - (1-r)^{-2.1}, & \text{for } K > 1 \end{cases} \tag{27}$$

where r is the maximum ratio defined by (17), and K is the number of independent spectra. By replacing (25) and (26) in (24), the following expressions are obtained:

$$s\tilde{Z}_{\mathrm{dr}}(k) = s\hat{Z}_{\mathrm{dr}}(k)\left\{1 - \frac{1}{\beta K}[1 - s\hat{\rho}^2_{\mathrm{HV}}(k)]\right\} \tag{28}$$

$$s\tilde{\rho}_{\mathrm{HV}}(k) = s\hat{\rho}_{\mathrm{HV}}(k)\left(1 - \frac{1}{\beta K}\left\{\frac{[1 - s\hat{\rho}^2_{\mathrm{HV}}(k)]^2}{4s\hat{\rho}^2_{\mathrm{HV}}(k)}\right\}\right) \tag{29}$$

where the tilde denotes the bias-corrected estimate.

IV. Performance of the Bootstrap DPSD Estimator

To properly demonstrate the advantages of the Bootstrap DPSD estimator, its statistical performance under different conditions is analyzed next. We consider single- and dual-signal cases, and evaluate the Bootstrap DPSD estimator with single or multiple dwells.

A. Methodology for Single-Signal Analysis

A dual-polarimetric extension of the weather-like signal simulator in [51] is used to study the performance of the estimators. Multiple realizations are produced to get K independent spectra, and the statistical properties of the estimator are computed using N iterations. This type of synthetic simulation allows generation of virtually any desired signal (or composite signal) under different scenarios, making it a powerful tool to study the statistical properties of any estimator. With this simulation procedure, the signal parameters that have a potential impact on the quality of the spectral estimates are SNR, M, σ_v, Z_{DR}, ρ_{HV}, and K. Throughout this section, the signal parameters are selected to resemble typical observations. The SNR is arbitrarily set high (20 dB) such that the noise contamination is minimal. While a Gaussian assumption for the simulated signals may not be the most realistic, it provides a simple model that can capture features of the signal such that quantitative performance analyses can be conducted.

The procedure to compute the statistical errors of the estimates is explained in Appendix A. Assuming the signal originates from a single group of uniform scatterers, for each set of independent estimates ($s\hat{Z}_{\mathrm{DR}}$ and $s\hat{\rho}_{\mathrm{HV}}$), the spectral coefficients above an SNR threshold are used to compute the average spectral errors. Herein, the bulk[1] radar variables are

[1] The term 'bulk' will be used to simply refer to the conventional variables, and to distinguish them from the spectral variables.

TABLE I
SIMULATION PARAMETERS FOR THE ANALYSIS OF THE ERRORS

Simulation parameter	Value
M	64
N	5000
$\bar{v}_{\mathrm{r}}$	$5\ \mathrm{m\,s^{-1}}$
σ_v	$2\ \mathrm{m\,s^{-1}}$
$\mathrm{SNR_V}$	30 dB
Z_{DR}	1.5 dB
ρ_{HV}	0.90
v_{a}	$15.7\ \mathrm{m\,s^{-1}}$

used as the true value to compute the errors, because the signal is modeled as such.

Studying the effect of each simulation parameter on the error quality over a wide range of values for all DPSD estimators under consideration would be lengthy, but a preliminary analysis [48] of the ideal estimator[2] was used to determine the parameters with higher impact on the errors. It was found that for high sSNR, the errors show significant dependence on $s\rho_{\mathrm{HV}}$ and K for spectral polarimetric variables [34].

B. Analysis of the Single-Dwell Estimator for the Single-Signal Case

The performance of the conventional and Bootstrap DPSD estimators is studied for a single signal, and the ideal estimator with $K = 20$ is selected as a standard for comparison. Additionally, the analysis focuses on the errors as a function of ρ_{HV} and for $K = 1$ (single dwell).

For a fair comparison between the different DPSD estimators, the parameters for the conventional methods are selected such that there is minimal frequency resolution loss and spectral smearing. That is, for Welch's estimator, the segment length is set to $L = M - 1$ with maximum overlap; and for Daniell's estimator, a three-point moving-average filter ($p = 1$) is used for PSD smoothing. The Bootstrap DPSD estimates are obtained using $K' = 20$ pseudorealizations. Unless otherwise noted, the analysis parameters are listed in Table I, with ρ_{HV} varying from 0.85 to 0.99. The data window for the analysis is a Blackman–Nuttall window, though it should be noted that other windows with sufficient sidelobe levels yield similar results.

The performance of the estimators in terms of the statistical errors as a function of the true correlation coefficient is shown in Fig. 2. The errors for Welch estimates (red line) with the best possible frequency resolution are extremely high and impractical for our purpose. It can be observed that the Bootstrap DPSD estimates (blue line) are better than Daniell estimates (green line) for all the cases. For $s\hat{Z}_{\mathrm{DR}}$, and $\rho_{\mathrm{HV}} = 0.90$, the Daniell estimator has a bias of 0.7014 dB, while the biases of the Bootstrap estimator and the ideal estimator are of 0.044 and 0.036 dB, respectively. The standard deviations (SDs) are 1.386, 0.803, and 0.210 dB, for the Daniell, Bootstrap, and ideal estimators, respectively. For the same $\rho_{\mathrm{HV}} = 0.90$, the normalized biases of $s\hat{\rho}_{\mathrm{HV}}$ are 0.0368, 0.0126, and 0.00002; and the normalized SDs are 0.0557,

[2]Hereafter, the periodogram DPSD estimator is the one that averages K independent periodogram PSD estimates, and the ideal DPSD estimator is the periodogram DPSD estimator with $K = 20$ independent spectra.

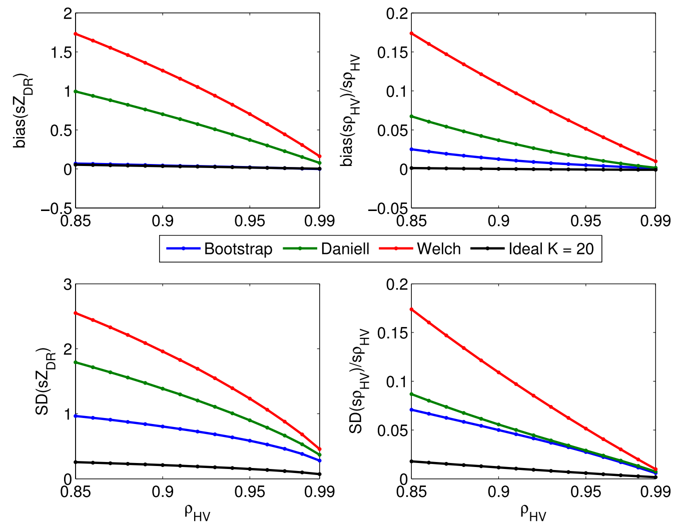

Fig. 2. Errors of the spectral polarimetric variables as a function of the true ρ_{HV} values. Bias (top-left) and SD (bottom-left) of $s\hat{Z}_{\mathrm{DR}}$, and normalized bias (top-right) and SD (bottom-right) of $s\hat{\rho}_{\mathrm{HV}}$ for $Z_{\mathrm{DR}} = 1.5$ dB. The Bootstrap DPSD (blue line), Daniell (green line), Welch (red line), and ideal with $K = 20$ (black line) estimates are compared.

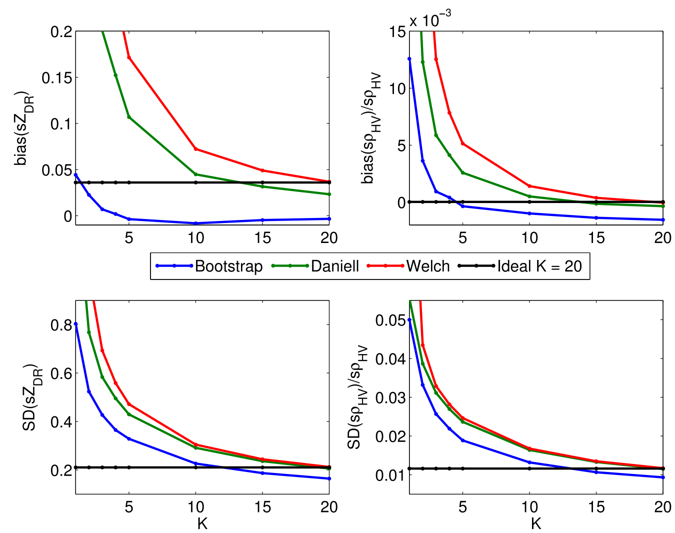

Fig. 3. Errors of the spectral polarimetric variables as a function of the number of independent dwells K for $\rho_{\mathrm{HV}} = 0.90$. Bias (top-left) and SD (bottom-left) of $s\hat{Z}_{\mathrm{DR}}$, normalized bias (top-right) and SD (bottom-right) of $s\hat{\rho}_{\mathrm{HV}}$. The Bootstrap (blue line), Daniell (green line), Welch (red line), and ideal (black line) estimators are shown for comparison.

0.0500, and 0.0116, for the Daniell, Bootstrap, and ideal estimators, respectively. A clear improvement in the quality of the DPSD estimates can be seen for the Bootstrap estimator over conventional methods, especially for the $s\hat{Z}_{\mathrm{DR}}$ bias. It is important to note that for higher ρ_{HV}, the errors of the Bootstrap estimates are closer to the error levels of the ideal estimator. However, for less coherent signals (i.e., lower ρ_{HV}), the quality of the estimates is degraded. Therefore, in practice, with single-dwell DPSD estimates using the Bootstrap DPSD estimator, a good qualitative analysis can be performed but the error levels may not be sufficient for a reliable quantitative analysis. Nonetheless, Section IV-C will show that the errors can be improved by using multiple dwells.

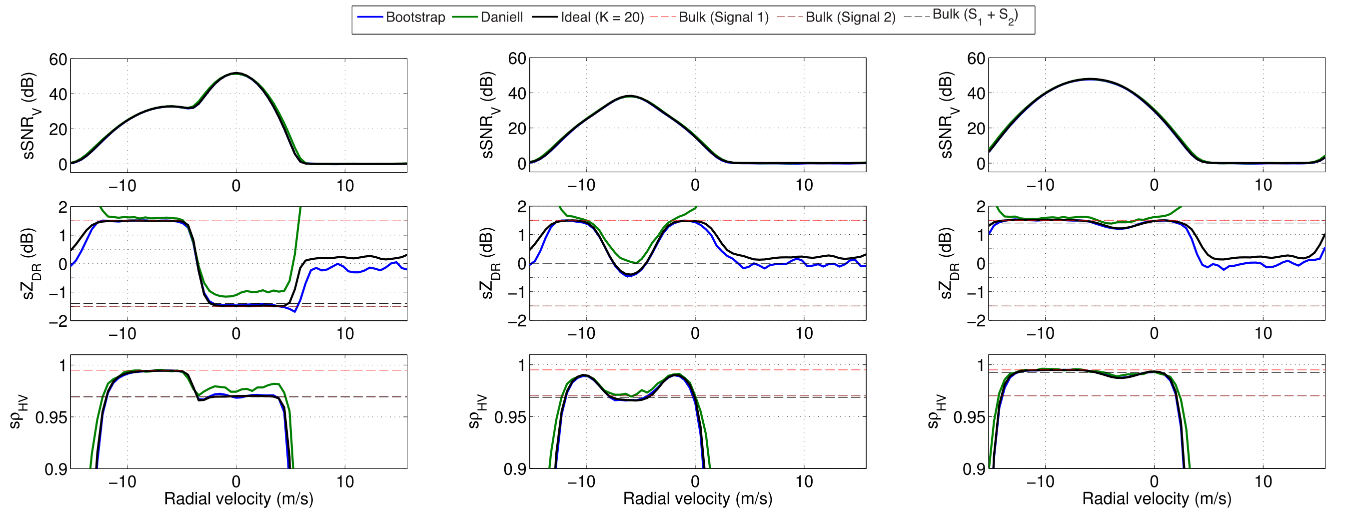

(a) (b) (c)

Fig. 4. Dual-signal analysis examples. Mean of the DPSD estimates of Bootstrap (blue line), Daniell (green line), and ideal (black line) estimates, and true bulk polarimetric variables of signal 1 (red dashed line) and signal 2 (dark red dashed line) are shown for (a) case 4, (b) case 5, and (c) case 10.

C. Analysis of the Multiple-Dwell Estimator for the Single-Signal Case

It is possible to obtain better error levels by averaging multiple spectra for DPSD estimation (i.e., $K \geq 2$) with the estimators under analysis. As mentioned previously, more spectra can be obtained from adjacent locations or consecutive scans, and it is important to keep the averaging in any of these dimensions to a minimum in order to avoid degrading the resolution. For this analysis, the statistical errors of conventional and Bootstrap DPSD estimators for $K \geq 2$ are compared with the ideal estimator, as shown in Fig. 3 (the same simulation parameters as before). For $\rho_{\mathrm{HV}} = 0.90$, the biases of the ideal estimator are equivalent to the Daniell estimator with $K \simeq 13, 14$, and the Bootstrap estimator with $K \simeq 3$. The Bootstrap DPSD estimator shows a significant improvement in the biases and in the reduction of the number of independent spectra needed. However, to meet the SD of the ideal estimates, a considerable number of independent spectra are still needed. The SDs for the ideal estimator are equivalent to the Daniell estimator with $K \simeq 20$ and the Bootstrap estimator with $K \simeq 13$. For the Daniell estimator, a marginal improvement is observed, while the Bootstrap estimator shows overall better performance. When $K > 20$, the Welch estimator converges with the ideal estimator, while the Daniell estimator performs marginally better, and the Bootstrap estimator exceeds the performance of the ideal estimator. One important drawback of the Bootstrap DPSD estimator is the inherent loss of coherence associated with the application of correction strategies, depicted in the negative biases of $s\hat{\rho}_{\mathrm{HV}}$ for larger K. Still, the normalized bias of $s\hat{\rho}_{\mathrm{HV}}$ is within 0.002 for $K \geq 2$ and for $\rho_{\mathrm{HV}} = 0.90$, which is within the error level recommended by [52]. While this limitation is noted, the Bootstrap DPSD estimator can generally achieve better quality estimates (for a given number of independent spectra) than conventional estimators.

TABLE II
SIGNAL PARAMETERS FOR DUAL-SIGNAL ANALYSIS CASES

	Signal 1				
Case	SNR (dB)	$\bar{v}_{\mathrm{r}}$ ($\mathrm{m\,s^{-1}}$)	σ_v ($\mathrm{m\,s^{-1}}$)	Z_{DR} (dB)	ρ_{HV}
0	25	-6	2	1.5	0.995
1 2 3 4	25	-6	2	1.5	0.995
5 6 7 8	25	-6	2	1.5	0.995
9 10 11 12	40	-6	2	1.5	0.995
	Signal 2				
Case	SNR (dB)	$\bar{v}_{\mathrm{r}}$ ($\mathrm{m\,s^{-1}}$)	σ_v ($\mathrm{m\,s^{-1}}$)	Z_{DR} (dB)	ρ_{HV}
0	40	9	1	-1.5	0.97
1 2 3 4	40	-6 -4 -2 0	1	-1.5	0.97
5 6 7 8	25	-6 -4 -2 0	1	-1.5	0.97
9 10 11 12	25	-6 -4 -2 0	1	-1.5	0.97

D. Methodology for Dual-Signal Analysis

As expected, there are various signal parameters that affect the ability to separate two different spectral signatures, including the difference between the mean radial velocities of the individual signals, their spectrum widths, the difference between the SNRs, and their polarimetric characteristics. To measure the performance of the DPSD estimators

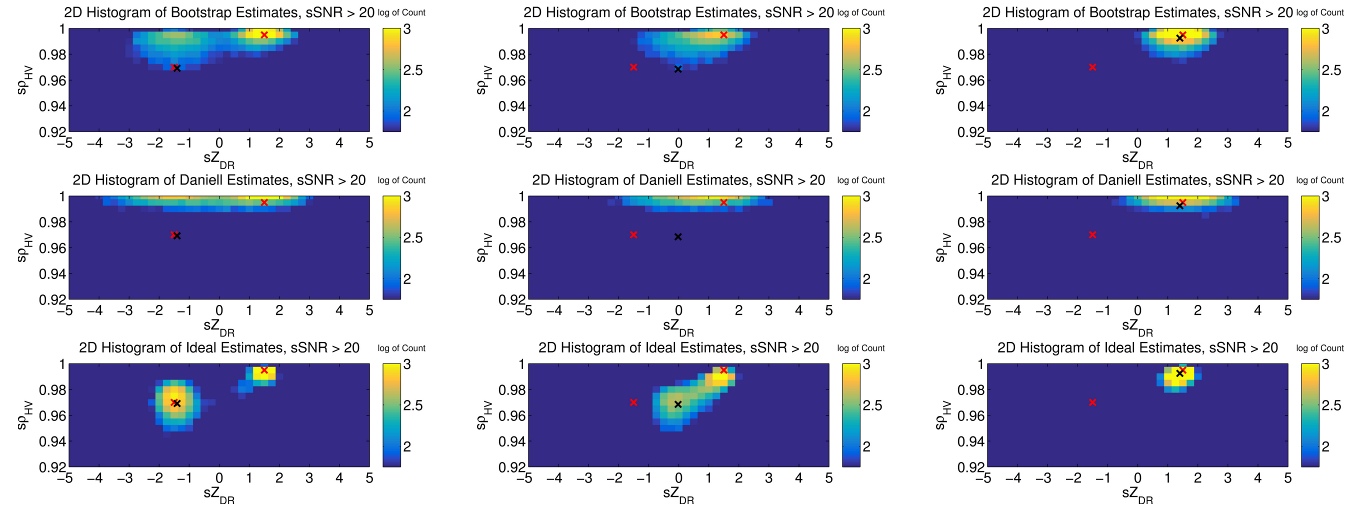

(a) (b) (c)

Fig. 5. Dual-signal analysis examples. Bivariate histograms of $s\hat{\rho}_{\mathrm{HV}}$ and $s\hat{Z}_{\mathrm{DR}}$ for thresholded spectral coefficients in logarithmic (log) scale of Bootstrap (top), Daniell (middle), and ideal (bottom) estimates, with $\times$ indicating the bulk estimates of the composite (black cross) and individual (red cross) signals, for (a) case 4, (b) case 5, and (c) case 10.

TABLE III

ABILITY TO DISTINGUISH SIGNAL CONSTITUENTS

Methods	Cases				
	1, 5, 9 ($\lvert\Delta\bar{v}_r\rvert = 0$)	2, 6, 10 ($\lvert\Delta\bar{v}_r\rvert = \sigma_{v,1}$)	3, 7, 11 ($\lvert\Delta\bar{v}_r\rvert = 2\sigma_{v,1}$)	4, 8, 12 ($\lvert\Delta\bar{v}_r\rvert = 3\sigma_{v,1}$)	0 ($\lvert\Delta\bar{v}_r\rvert > 3\sigma_{v,1}$)
Daniell	None	None	1 out of 3 (sZ_{DR} only)	1 out of 3 (sZ_{DR} only)	All
Bootstrap	1 out of 3	1 out of 3	2 out of 3	All	All
Ideal	2 out of 3	2 out of 3	All	All	All

when discriminating different signals in the spectra, 13 cases were simulated, each containing two signals with different polarimetric characteristics and several degrees of mixing. Signal 1 is assumed to be a highly coherent signal with values resembling those of typical raindrops, while signal 2 is less coherent with negative Z_{DR} resembling hypothetical tornadic debris. Although a Gaussian assumption for debris signals is not realistic, it serves to illustrate the presence of signals with different polarimetric characteristics in the spectra, as will be shown in the following cases. The parameters for the signals used hereafter are summarized in Table II, with $N = 1000$ iterations. In case 0, the difference in mean radial velocities is sufficiently large and the spectrum widths are moderately wide, such that there is almost no overlap between the signals. For cases 1–4, the hypothetical debris signal is assumed to be higher in power, and its mean radial velocity is varied such that the difference in radial velocity is 0, $\sigma_{v,1}$, $2\sigma_{v,1}$, and $3\sigma_{v,1}$, for cases 1–4, respectively. Cases 5–9 assume the raindrop and the debris signals are comparable in power, with the difference in radial velocities varied as with the previous case set. The same is done for cases 9–12, but the raindrop signal has higher power.

E. Analysis of the Single-Dwell Estimator for the Dual-Signal Case

The average of $N = 1000$ iterations for select cases is shown in Fig. 4(a)–(c), for the Bootstrap ($K = 1$), Daniell ($K = 1$), and ideal ($K = 20$) estimators. Additionally, the values for the true bulk polarimetric variables for the signals are plotted in dashed lines. In Fig. 5(a)–(c), a 2-D histogram (hereafter, histogram) of $s\hat{\rho}_{\mathrm{HV}}$ and $s\hat{Z}_{\mathrm{DR}}$, for corresponding cases, is computed for the thresholded spectral coefficients over $N = 1000$ iterations, in logarithmic (log) scale. Red markers indicate the true values of the signals, while black markers indicate the bulk estimate of the composite signal. It is important to note that the distributions are skewed toward high $s\rho_{\mathrm{HV}}$, but the mean values depicted in the DPSD estimates are in fact closer to the markers in the histograms than it appears. The logarithmic scale was chosen to emphasize the distributions of the polarimetric characteristics of the SNR-thresholded spectral coefficients, since the mean values of the DPSD estimates may not always correctly represent important differences in features between the estimators under analysis. The error statistics for each individual signal, in every case, are equivalent to those of the single-signal analysis.

In general, the ability to successfully discriminate different signals in the spectrum is related to the difference in their mean radial velocities, power ratio, and spectrum widths, since these factors determine the shape of the power spectrum. Cases with bimodal spectra [e.g., case 4, shown in Fig. 4(a) and 5(a)] were found to have higher success in discrimination than cases with unimodal spectra with different polarimetric characteristics [e.g., case 5, shown in Fig. 4(b) and 5(b)], because the degree of overlap of the spectral components of the different signals is lower. In either case, techniques, such as filtering of nondesired signals, could be used to further

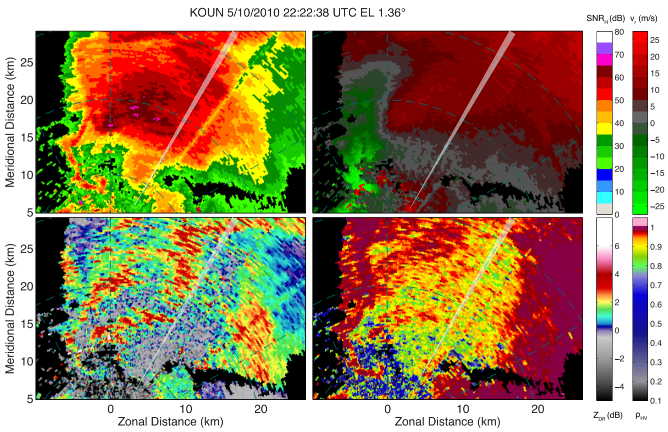

Fig. 6. PPI plots corresponding to KOUN data at 22:22:38 UTC, and elevation $\phi = 1.36°$ with azimuth $\theta = 30°$ highlighted. (Top-left) $\mathrm{SNR_H}$. (Top-right) $\bar{v}_r$. (Bottom-left) Z_{DR}. (Bottom-right) ρ_{HV}. Grid lines are 30° and 10 km apart.

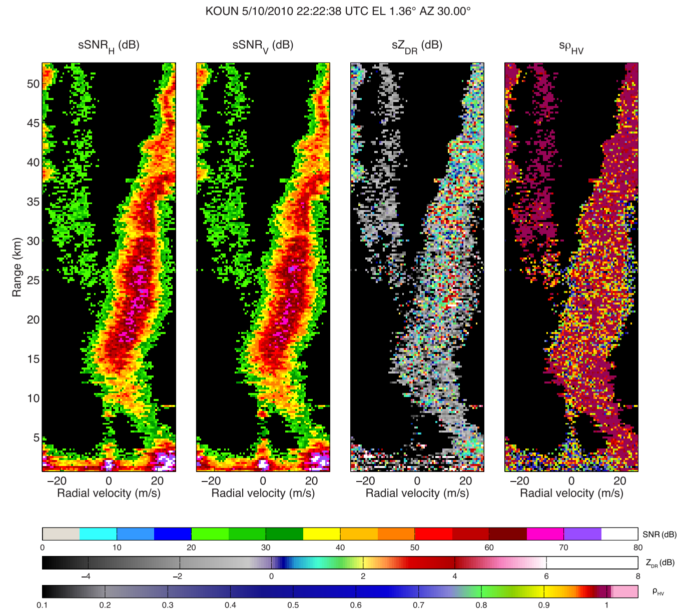

Fig. 7. Range-Doppler plots of single-dwell Bootstrap DPSD estimates corresponding to KOUN data at 22:22:38 UTC, elevation $\phi = 1.36°$, azimuth $\theta = 30°$, and ranges 0.75 to 52.5 km, of (from left to right) estimates of spectral SNR of the H and V channels ($s\mathrm{SNR_H}$ and $s\mathrm{SNR_V}$), spectral differential reflectivity (sZ_{DR}), and spectral correlation coefficient ($s\rho_{\mathrm{HV}}$).

improve the accuracy of the bulk estimates of the desired signal. In unimodal cases with a dominant signal [e.g., case 10, shown in Fig. 4(c) and 5(c)], there may exist subtle indications of the presence of a nondominant signal in the spectrum. However, any meaningful quantitative information about the masked signal is lost (e.g., wide high-power signal completely masking a narrow weaker signal, signals of similar widths and mean radial velocities, signals with similar polarimetric characteristics and mean radial velocities, and so on) and discrimination may be impossible even with an ideal DPSD estimator.

A summary of the results of the dual-signal analysis is presented in Table III. Here, a successful separation in the histogram means that the polarimetric characteristics of two distinct signals were qualitatively evident for these cases. The Daniell estimates performed poorly in most cases due to the high bias and variance of its estimates. In 8 out of the 13 cases under analysis, the Bootstrap estimates showed distinct distributions near the true Z_{DR} values of the signals, though with a somewhat skewed distribution in $s\hat{\rho}_{\mathrm{HV}}$ with a mean bias similar to the values from the single-signal, single-dwell analysis. Likewise, the ideal estimates were slightly more successful with 11 out of 13 cases. In the three cases, where the Bootstrap estimate performance was inferior to the ideal estimates, it was found that a proper separation of the signals was not possible due to the high variance. Furthermore, in two cases where a wider and stronger signal was completely dominating the weaker signal, none of the estimators were able to identify the distinct spectral signatures.

V. Results on Observations

The following analysis uses I/Q time-series data collected with the KOUN radar during the May 10, 2010 Moore–Norman, OK tornado. KOUN is an S-band polarimetric radar with a 0.9° 3-dB beamwidth, range sampling of 250 m, and a peak transmit power of 750 kW; on these dates, it operated with a maximum unambiguous velocity of 27.5 m s^{-1}. This case took part in the second largest single-day tornado outbreak documented in Oklahoma, which affected a large part of northern, central, and southern portions of the state. In-depth analyses based on weather radar observations of the May 10, 2010 case can be found in [17]. According to [53], during the late afternoon and early evening hours of this day, 13 different storms produced tornadoes, spawning a total of 36 tornadoes in the National Weather Service (NWS) Norman forecast area alone, and also producing significant structural damage over many areas with estimated losses in excess of \$595 million, three fatalities, and over 450 injuries. It is indicated that due to the potent combination of atmospheric conditions, the storms that developed quickly became tornadic after initiation, with typical storm motions of 50 to 60 mph (80.5 to 96.6 km h^{-1}). Reports indicate that between 22:33 and 22:59 UTC, three to five tornadoes were occurring simultaneously every minute, which includes two EF-4 tornadoes (the Moore and Norman tornadoes), and two other EF-3 tornadoes. Additionally, very large hail was reported in several locations with sizes up to 10.8 cm (4.25") in diameter (softball size). A detailed report of this event can be found in [53]. Some examples of polarimetric spectral signatures estimated with the Bootstrap DPSD estimator that are not captured by the bulk polarimetric variables are provided next.

The scan corresponding to 22:22:38 UTC with an elevation angle of 1.36° was selected and the PPIs are shown in Fig. 6. The data were grouped into 2.0° radials with a 0.5° azimuthal spacing, yielding approximately 79 samples per dwell. Range-Doppler plots are useful for spectral analysis, as they illustrate spectral variables as a function of range and radial velocity, with the intensity representing the particular spectral variable. Each row in the y-axis of the range-Doppler plots represents the spectrum for a given range location, and the

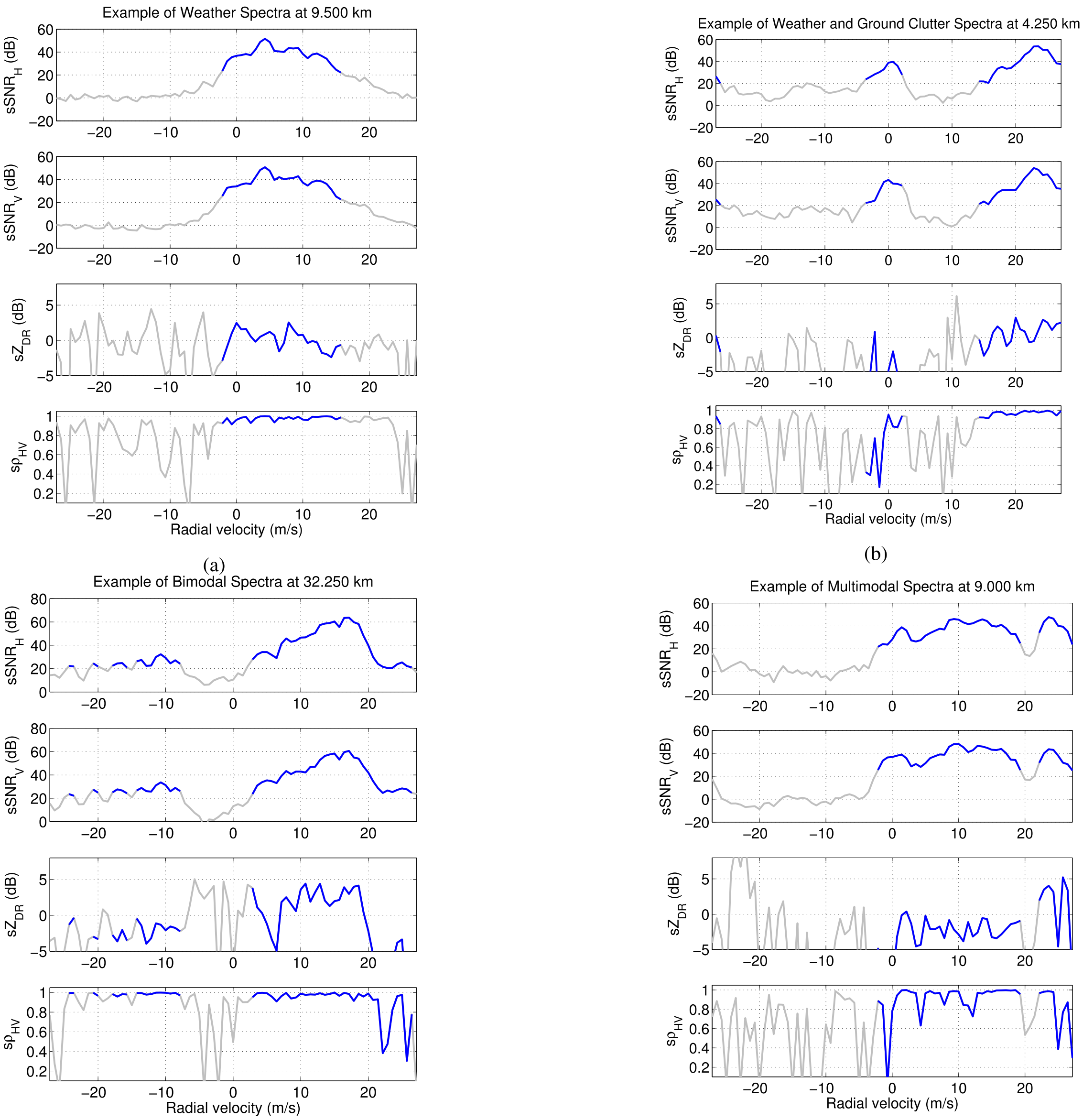

(a) (b) (c) (d)

Fig. 8. Plots of Bootstrap DPSD estimates [from top to bottom, estimates of spectral SNR of the H and V channels ($s\mathrm{SNR_H}$ and $s\mathrm{SNR_V}$), spectral differential reflectivity (sZ_{DR}), and spectral correlation coefficient ($s\rho_{\mathrm{HV}}$)] corresponding to KOUN data at 22:22:38 UTC, elevation $\phi = 1.36°$, and azimuth $\theta = 30°$. (a) Weather signature at 9.5 km. (b) Weather and ground clutter signature at 4.25 km. (c) Bimodal spectra at 32.25 km. (d) Multimodal spectra at 9 km. The spectral components above a threshold of $s\mathrm{SNR_H} > 20$ dB and $s\mathrm{SNR_V} > 20$ dB are highlighted in blue, while the components below this threshold are shaded in gray.

x-axis represents the radial velocity. With the aid of range-Doppler plots, it is possible to observe the spatial distribution and radar-relative motion of the scatterers in a particular ray, and with the DPSDs, it is also possible to detect any significantly different scatterer signatures for given radar resolution volumes. By computing the DPSD estimates, distinct spectral signatures can be found near azimuth $\theta = 30°$, as shown in Fig. 7. The DPSDs were estimated with a Blackman window, with no zero-padding for the DFT. Furthermore, a 20-dB SNR threshold is used to censor low-SNR spectral coefficients.

Typical features, such as unimodal weather signal and bimodal weather-plus-ground-clutter, are readily apparent in the DPSD plots [Fig. 8(a) and (b)]. The weather signal has a unimodal distribution with differences in sZ_{DR}, which may be attributed to smaller raindrops being centrifuged or size sorting. Moreover, between 10 and 15 m s^{-1}, the DPSDs show negative $s\hat{Z}_{\mathrm{DR}}$ and relatively high $s\hat{\rho}_{\mathrm{HV}}$, which could be attributed to debris particles that are smaller than a wavelength in size. For the example of weather mixed with ground clutter, the hydrometeors are moving with a mean radial velocity of approximately 22.5 m s^{-1} with positive $s\hat{Z}_{\mathrm{DR}}$ and high $s\hat{\rho}_{\mathrm{HV}}$; while the ground clutter signal is shown with a zero mean radial velocity, negative $s\hat{Z}_{\mathrm{DR}}$, and low $s\hat{\rho}_{\mathrm{HV}}$. Other interesting signatures are the bimodal signal spanning from approximately 20 to over 50 km in range, and a multimodal signal composed of weather, ground clutter, and an isolated peak at approximately 8 km. The DPSDs of these signatures are shown in Fig. 8(c) and (d). While it is difficult to provide a precise explanation for these observations, some hypotheses can be elaborated. A weaker signal of low sZ_{DR} is observed within a bimodal spectrum [Fig. 8(c)], along with a stronger weather signal with varying sZ_{DR} values and relatively high $s\rho_{\mathrm{HV}}$ values. Although the weaker signal has high $s\rho_{\mathrm{HV}}$ values, this may be due to the fact that these presumably nonhydrometeor scatterers might be small in size such that the volumetric scattering is mostly homogeneous. Another plausible explanation is that the weaker signal corresponds to a range-folded echo, as evidence of range folding was observed in the vicinity of the ray under analysis in later PPI scans for the same data set. If such were the case, the range-folded echoes could be mitigated with polarimetric spectral analysis, showing another important potential application of the Bootstrap DPSD estimator. For the last example, a signal with multiple peaks in the spectrum [Fig. 8(d)] can be observed in range locations near 8 km. The peak at approximately 2 m s^{-1} corresponds to weather, with sZ_{DR} values close to 0 (small raindrops) and high $s\rho_{\mathrm{HV}}$. A wider signal with negative sZ_{DR} and varying values of $s\rho_{\mathrm{HV}}$ can be seen from approximately 5 to 19 m s^{-1}. It is hypothesized that the polarimetric characteristics of this spectral signature may be attributed to debris, where the spectral components with high $s\hat{\rho}_{\mathrm{HV}}$ indicate homogeneous scattering, and the low $s\hat{\rho}_{\mathrm{HV}}$ indicate nonhomogeneous scattering from groups of different types of debris. And also, an isolated peak of a scatterer with high sZ_{DR} and high $s\rho_{\mathrm{HV}}$ with a motion of over 20 m s^{-1} can be seen in the spectra. This unknown scatterer could be a group of relatively large pieces of debris being lofted in the air, and a hypothesis for the velocity being higher than the surrounding wind could be explained if the object was ejected radially in the direction of the radar beam with a higher tangential velocity. Alternatively, since ground clutter contamination is still present at this elevation angle and range, the echo could correspond to a moving vehicle. It is important to note that these characteristics can be appreciated even with single-dwell DPSDs, showing the potential of the Bootstrap DPSD estimator in different spectral analysis applications.

VI. Conclusion

Bulk radar estimates depict useful information about the characteristics and motion of weather phenomena. However, these measurements are susceptible to biases when the signal of interest is contaminated by other types of scatterers in the radar volume. The DPSDs may unveil additional information for the groups of scatterers moving at different Doppler velocities, which can potentially aid in the characterization of distinct scatterer types. Identification of different polarimetric spectral signatures is important for many applications. For example, by discriminating hydrometeors in spectra, it should be possible to obtain more accurate wind velocity measurements, which is very important for tornado intensity and damage potential estimation. Previous DPSD estimation methods required averaging $K \geq 20$ spectra to get estimates with desirable error levels; a number of spectra could be obtained from adjacent locations or consecutive scans. A smaller number of spectra could be averaged, though the quality of the estimates is usually insufficient for quantitative spectral analyses. Additionally, good resolution is required in all dimensions in order to capture important features of meteorological phenomena that evolve relatively fast in time, in a small spatial extent, and with scatterers moving at different velocities within the radar volume (e.g., tornadoes).

The Bootstrap DPSD estimator was introduced as a means to compute the DPSDs from a single dwell with minimal resolution loss. It employs the bootstrap resampling concept, which is a useful method to measure statistical properties of estimators when the available sample size is small. Briefly, the estimator preprocesses and then bootstraps the conditioned I/Q time-series signals to obtain I/Q pseudorealizations, which are in turn used to obtain bootstrapped PSD estimates. The DPSDs are then computed by averaging the bootstrapped estimates, and a bias correction is applied to obtain the final estimates. The pre and postprocessing strategies, as well as the appropriate selection of parameters are at the core of the design of the Bootstrap DPSD estimator. The Bootstrap DPSD estimator shows superior error statistics when compared with conventional DPSD estimators for single dwell as well as for multiple-dwell estimates, and it was shown that it meets the performance of the ideal estimator with about half the number of averaged independent spectra. However, the Bootstrap DPSD estimator has a particular limitation in that, by attempting to correct the signal coherency, it can introduce a small bias in the spectral correlation coefficient estimates. Further analyses of the impacts of this limitation are needed. Additionally, the Bootstrap DPSD estimator shows better performance than the conventional DPSD estimators when discriminating polarimetric signatures of signals corresponding to different groups of scatterers moving at different radial velocities in the radar volume. However, the ideal (but impractical) estimator still outperforms the single-dwell Bootstrap DPSD estimator in the dual-signal analysis. Though a multiple dwell, dual-signal analysis was not conducted, it is expected that the Bootstrap DPSD estimator will have superior performance compared with both the conventional and the ideal DPSD estimators.

The potential of the Bootstrap DPSD estimator was demonstrated with a few representative examples using data from a real tornado case. It was illustrated in the examples how polarimetric spectral analyses can unveil additional information obscured by bulk estimates. It is expected that the spectral analysis can provide more insight to better understand tornado dynamics and their connection to weather radar measurements. However, to validate the observations from a physical point of view and to answer the scientific questions that motivated this paper, more in-depth analyses are required. Such studies are beyond the scope of this paper.

Appendix A
Single-Signal Statistical Error Calculation

The average value of the SNR-thresholded spectral coefficients represents the strong signal components with minimal noise. These are obtained as

$$\overline{s\hat{Z}_{\mathrm{dr}}} = \langle s\hat{Z}_{\mathrm{dr}}(k')\rangle \tag{A1}$$

$$\overline{s\hat{\rho}_{\mathrm{HV}}} = \langle s\hat{\rho}_{\mathrm{HV}}(k')\rangle \tag{A2}$$

where k' values are the spectral coefficients for which $s\hat{\mathrm{SNR}}_{\mathrm{H}}$ and $s\hat{\mathrm{SNR}}_{\mathrm{V}}$ are greater than 20 dB, and $\langle\cdot\rangle$ indicates averaging in the frequency domain. The bias of $s\hat{Z}_{\mathrm{DR}}$ is then obtained as

$$\begin{aligned}\mathrm{bias}(s\hat{Z}_{\mathrm{dr}}) &= E[\overline{s\hat{Z}_{\mathrm{dr}}} - Z_{\mathrm{dr}}]\\ &\simeq \frac{1}{N}\sum_{n=0}^{N-1}(\overline{s\hat{Z}_{\mathrm{dr},n}} - Z_{\mathrm{dr}}) \end{aligned}\tag{A3}$$

$$\mathrm{bias}(s\hat{Z}_{\mathrm{DR}}) = 10\log\left[1 + \frac{\mathrm{bias}(s\hat{Z}_{\mathrm{dr}})}{Z_{\mathrm{dr}}}\right] (\mathrm{dB}) \tag{A4}$$

where N is the number of iterations (independent DPSDs) used to study the statistical variability of the spectral estimates, not to be confused with the K independent spectra used to compute the DPSDs. The SD of $s\hat{Z}_{\mathrm{DR}}$ is computed as

$$\begin{aligned}\mathrm{SD}(s\hat{Z}_{\mathrm{dr}}) &= \sqrt{E[(\overline{s\hat{Z}_{\mathrm{dr}}} - Z_{\mathrm{dr}})^2]}\\ &\simeq \sqrt{\frac{1}{N}\sum_{n=0}^{N-1}(\overline{s\hat{Z}_{\mathrm{dr},n}} - Z_{\mathrm{dr}})^2} \end{aligned}\tag{A5}$$

$$\mathrm{SD}(s\hat{Z}_{\mathrm{DR}}) = 10\log\left[1 + \frac{\mathrm{SD}(s\hat{Z}_{\mathrm{dr}})}{Z_{\mathrm{dr}}}\right] (\mathrm{dB}). \tag{A6}$$

The normalized bias and SD of $s\hat{\rho}_{\mathrm{HV}}$ are

$$\begin{aligned}\frac{\mathrm{bias}(s\hat{\rho}_{\mathrm{HV}})}{\rho_{\mathrm{HV}}} &= \frac{E[\overline{s\hat{\rho}_{\mathrm{HV}}} - \rho_{\mathrm{HV}}]}{\rho_{\mathrm{HV}}}\\ &\simeq \frac{\frac{1}{N}\sum_{n=0}^{N-1}(\overline{s\hat{\rho}_{\mathrm{HV},n}} - \rho_{\mathrm{HV}})}{\rho_{\mathrm{HV}}} \end{aligned}\tag{A7}$$

$$\begin{aligned}\frac{\mathrm{SD}(s\hat{\rho}_{\mathrm{HV}})}{\rho_{\mathrm{HV}}} &= \frac{\sqrt{E[(\overline{s\hat{\rho}_{\mathrm{HV}}} - \rho_{\mathrm{HV}})^2]}}{\rho_{\mathrm{HV}}}\\ &\simeq \frac{\sqrt{\frac{1}{N}\sum_{n=0}^{N-1}(\overline{s\hat{\rho}_{\mathrm{HV},n}} - \rho_{\mathrm{HV}})^2}}{\rho_{\mathrm{HV}}}. \end{aligned}\tag{A8}$$

Equations (A3)–(A8) are used to quantify the dependence on the different parameters under analysis.

ACKNOWLEDGMENT

The authors would like to thank Dr. C. Fulton for his input in the design of the coherency correction factor.

REFERENCES

[1] J. J. Bohonos and D. E. Hogan, "The medical impact of Tornadoes in North America," *J. Emergency Med.*, vol. 17, no. 1, pp. 67–73, Jan./Feb. 1999.

[2] T. P. Marshall, "Tornado damage survey at Moore, Oklahoma," *Weather Forecasting*, vol. 17, no. 3, pp. 582–598, 2002.

[3] National Weather Service (NWS) Office of Climate, Water, and Weather Services, and the National Climatic Data Center (NCDC), "Summary of natural hazard statistics for 2013 in the United States," Nat. Oceanic Atmospheric Administration (NOAA)/Nat. Weather Service (NWS), Silver Spring, MD, USA, Tech. Rep., May 2016. [Online]. Available: http://www.nws.noaa.gov/om/hazstats/sum13.pdf

[4] P. Markowski and Y. Richardson, "What we know and don't know about Tornado formation," *Phys. Today*, vol. 67, no. 9, pp. 26–31, 2014.

[5] J. Wurman, K. Kosiba, and P. Robinson, "*In Situ*, Doppler radar, and video observations of the interior structure of a Tornado and the Wind–Damage relationship," *Bull. Amer. Meteorol. Soc.*, vol. 94, no. 6, pp. 835–846, 2013.

[6] R. J. Doviak, V. Bringi, A. V. Ryzhkov, A. Zahrai, and D. S. Zrnić, "Considerations for polarimetric upgrades to operational WSR-88D radars," *J. Atmos. Ocean. Technol.*, vol. 17, no. 3, pp. 257–278, 2000.

[7] D. J. Bodine, R. D. Palmer, T. Maruyama, C. J. Fulton, Y. Zhu, and B. L. Cheong, "Simulated frequency dependence of radar observations of Tornadoes," *J. Atmos. Ocean. Technol.*, vol. 33, no. 9, pp. 1825–1842, 2016. [Online]. Available: http://journals.ametsoc.org/doi/10.1175/JTECH-D-15-0120.1

[8] A. V. Ryzhkov, T. J. Schuur, D. W. Burgess, and D. S. Zrnić, "Polarimetric Tornado detection," *J. Appl. Meteorol.*, vol. 44, no. 5, pp. 557–570, 2005.

[9] A. V. Ryzhkov, D. W. Burgess, D. S. Zrnić, T. Smith, and S. E. Giangrande, "Polarimetric analysis of a 3, May 1999 Tornado," in *Proc. 21st Conf. Severe Local Storms*, vol. 14. San Antonio, TX, USA, 2002, pp. 515–518, paper 14.2.

[10] D. C. Dowell, C. R. Alexander, J. M. Wurman, and L. J. Wicker, "Centrifuging of hydrometeors and debris in Tornadoes: Radar-reflectivity patterns and wind-measurement errors," *Monthly Weather Rev.*, vol. 133, no. 6, pp. 1501–1524, 2005.

[11] M. R. Kumjian and A. V. Ryzhkov, "Polarimetric signatures in supercell thunderstorms," *J. Appl. Meteorol. Climatol.*, vol. 47, no. 7, pp. 1940–1961, Jul. 2008.

[12] C. J. Schultz *et al.*, "Dual-polarization tornadic debris signatures part I: Examples and utility in an operational setting," *Electron. J. Oper. Meteorol.*, vol. 13, no. 9, pp. 120–137, 2012.

[13] C. J. Schultz *et al.*, "Dual-polarization tornadic debris signatures part II: Comparisons and caveats," *Electron. J. Oper. Meteorol.*, vol. 13, no. 10, pp. 138–150, 2012.

[14] K. A. Scharfenberg *et al.*, "The joint polarization experiment: Polarimetric radar in forecasting and warning decision making," *Weather Forecasting*, vol. 20, no. 5, pp. 775–788, 2005.

[15] D. J. Bodine, M. R. Kumjian, R. D. Palmer, P. L. Heinselman, and A. V. Ryzhkov, "Tornado damage estimation using polarimetric radar," *Weather Forecasting*, vol. 28, no. 1, pp. 139–158, 2013.

[16] H. B. Bluestein *et al.*, "Close-range observations of Tornadoes in supercells made with a dual-polarization, X-band, mobile Doppler radar," *Monthly Weather Rev.*, vol. 135, no. 4, pp. 1522–1543, Apr. 2007.

[17] R. D. Palmer *et al.*, "Observations of the 10, May 2010 Tornado outbreak using OU-PRIME: Potential for new science with high-resolution polarimetric radar," *Bull. Amer. Meteorol. Soc.*, vol. 92, no. 7, pp. 871–891, 2011.

[18] R. J. Doviak and D. S. Zrnić, *Doppler Radar and Weather Observations*, 2nd ed. New York, NY, USA: Dover, 2006.

[19] L. H. Janssen and G. A. Van Der Spek, "The shape of Doppler spectra from precipitation," *IEEE Trans. Aerosp. Electron. Syst.*, vol. AES-21, no. 2, pp. 208–219, Mar. 1985.

[20] T.-Y. Yu, R. R. Rondinel, and R. D. Palmer, "Investigation of non-Gaussian Doppler spectra observed by weather radar in a tornadic supercell," *J. Atmos. Ocean. Technol.*, vol. 26, no. 3, pp. 444–461, 2009.

[21] S. M. Torres and D. S. Zrnić, "Ground clutter canceling with a regression filter," *J. Atmos. Ocean. Technol.*, vol. 16, no. 10, pp. 1364–1372, 1999.

[22] Q. Cao, G. Zhang, R. D. Palmer, M. Knight, R. May, and R. J. Stafford, "Spectrum-time estimation and processing (STEP) for improving weather radar data quality," *IEEE Trans. Geosci. Remote Sens.*, vol. 50, no. 11, pp. 4670–4683, Nov. 2012.

[23] S. M. Torres and D. A. Warde, "Ground clutter mitigation for weather radars using the autocorrelation spectral density," *J. Atmos. Ocean. Technol.*, vol. 31, no. 10, pp. 2049–2066, Oct. 2014.

[24] S. M. Bachmann and D. S. Zrnić, "Spectral density of polarimetric variables separating biological scatterers in the VAD display," *J. Atmos. Ocean. Technol.*, vol. 24, no. 7, pp. 1186–1198, 2007.

[25] D. N. Moisseev and V. Chandrasekar, "Polarimetric spectral filter for adaptive clutter and noise suppression," *J. Atmos. Ocean. Technol.*, vol. 26, no. 2, pp. 215–228, 2009.

[26] L. Alku, D. N. Moisseev, T. Aittomäki, and V. Chandrasekar, "Identification and suppression of nonmeteorological echoes using spectral polarimetric processing," *IEEE Trans. Geosci. Remote Sens.*, vol. 53, no. 7, pp. 3628–3638, Jul. 2015.

[27] C. Unal, "Spectral polarimetric radar clutter suppression to enhance atmospheric echoes," *J. Atmos. Ocean. Technol.*, vol. 26, no. 9, pp. 1781–1797, 2009.

[28] F. Yanovsky, "Inferring microstructure and turbulence properties in rain through observations and simulations of signal spectra measured with Doppler–polarimetric radars," in *Polarimetric Detection, Characterization and Remote Sensing*, M. I. Mishchenko, Y. S. Yatskiv, V. K. Rosenbush, and G. Videen, Eds. Dordrecht, The Netherlands: Springer, 2011, pp. 501–542.

[29] Y. Dufournet, "Ice crystal properties retrieval using radar spectral polarimetric measurements within ice/mixed-phase clouds," Ph.D. dissertation, Telecommun. Elect. Eng., Math. Comput. Sci., Delft Univ. Technol., Delft, The Netherlands, 2010.

[30] A. L. J. Spek, C. M. H. Unal, D. N. Moisseev, H. W. J. Russchenberg, V. Chandrasekar, and Y. Dufournet, "A new technique to categorize and retrieve the microphysical properties of ice particles above the melting layer using radar dual-polarization spectral analysis," *J. Atmos. Ocean. Technol.*, vol. 25, no. 3, pp. 482–497, 2008.

[31] D. N. Moisseev, V. Chandrasekar, C. M. H. Unal, and H. W. J. Russchenberg, "Dual-polarization spectral analysis for retrieval of effective raindrop shapes," *J. Atmos. Ocean. Technol.*, vol. 23, no. 12, pp. 1682–1695, 2006.

[32] D. N. Moisseev and V. Chandrasekar, "Nonparametric estimation of raindrop size distributions from dual-polarization radar spectral observations," *J. Atmos. Ocean. Technol.*, vol. 24, no. 6, pp. 1008–1018, 2007.

[33] T.-Y. Yu, H. Le, Y. Wang, A. V. Ryzhkov, and M. R. Kumjian, "Application of spectral polarimetry to a hailstorm at low elevation angle," in *Proc. 36th Conf. Radar Meteorol.*, Breckenridge, CO, USA, 2013, pp. 1–11, paper 13A.3.

[34] T.-Y. Yu, X. Xiao, and Y. Wang, "Statistical quality of spectral polarimetric variables for weather radar," *J. Atmos. Ocean. Technol.*, vol. 29, no. 9, pp. 1221–1235, 2012.

[35] F. J. Harris, "On the use of windows for harmonic analysis with the discrete Fourier transform," *Proc. IEEE*, vol. 66, no. 1, pp. 51–83, Jan. 1978.

[36] P. D. Welch, "The use of fast Fourier transform for the estimation of power spectra: A method based on time averaging over short, modified periodograms," *IEEE Trans. Audio Electroacoust.*, vol. 15, no. 2, pp. 70–73, Jun. 1967.

[37] P. Stoica and R. L. Moses, *Introduction to Spectral Analysis*. Upper Saddle River, NJ, USA: Prentice-Hall, 1997.

[38] P. J. Daniell, "Discussion on symposium on autocorrelation in time series," *J. Roy. Statist. Soc.*, vol. 8, no. 1, pp. 88–90, 1946.

[39] S. M. Torres and C. D. Curtis, "Design considerations for improved Tornado detection using super-resolution data on the NEXRAD network," in *Proc. 3rd Eur. Conf. Radar Meteorol. Hydrol. (ERAD)*, Barcelona, Spain, 2006, pp. 1–4.

[40] H. B. Bluestein, C. C. Weiss, and A. L. Pazmany, "Mobile Doppler radar observations of a Tornado in a supercell near Bassett, Nebraska, on 5 June 1999. Part I: Tornadogenesis," *Monthly Weather Rev.*, vol. 131, no. 12, pp. 2968–2984, 2003.

[41] H. B. Bluestein, M. M. French, I. Popstefanija, R. T. Bluth, and J. B. Knorr, "A mobile, phased-array doppler radar for the study of severe convective StormsTHE MWR-05XP," *Bull. Amer. Meteorol. Soc.*, vol. 91, no. 5, pp. 579–600, 2010.

[42] B. Efron, "Bootstrap methods: Another look at the jackknife," *Ann. Statist.*, vol. 7, no. 1, pp. 1–26, 1979.

[43] P. Hall, *The Bootstrap Edgeworth Expansion*. New York, NY, USA: Springer-Verlag, 1992.

[44] B. Efron and R. J. Tibshirani, *An Introduction to Bootstrap*. Boca Raton, FL, USA: CRC Press, 1994.

[45] A. M. Zoubir and R. D. Iskander, *Bootstrap Techniques for Signal Processing*. Cambridge, U.K.: Cambridge Univ. Press, 2004.

[46] H. Varian, "Bootstrap tutorial," *Math. J.*, vol. 9, no. 4, pp. 768–775, 2005.

[47] S. N. Lahiri, *Resampling Methods for Dependent Data*. New York, NY, USA: Springer-Verlag, 2003.

[48] A. Y. Umeyama, "The bootstrap dual polarimetric spectral density estimator," M.S. thesis, Dept. College Eng., School Elect. Comput. Eng., Univ. Oklahoma, Norman, OK, USA, 2016.

[49] H. R. Künsch, "The jackknife and the bootstrap for general stationary observations," *Ann. Statist.*, vol. 17, no. 3, pp. 1217–1241, Sep. 1989.

[50] R. Y. Liu and K. Singh, "Moving blocks jackknife and bootstrap capture weak dependence," in *Exploring Limits Bootstrap*, R. LePage and Y. Billard, Eds. New York, NY, USA: Wiley, 1992, pp. 225–248.

[51] D. S. Zrnić, "Simulation of weatherlike Doppler spectra and signals," *J. Appl. Meteorol.*, vol. 14, no. 4, pp. 619–620, 1975.

[52] V. M. Melnikov and D. S. Zrnic, "Simultaneous transmission mode for the polarimetric WSR-88D: Statistical biases and standard deviations of polarimetric variables," NOAA Nat. Severe Storms Lab. (NSSL) CIMMS Report, Cooperative Inst. Mesoscale Meteorol. Studies (CIMMS), Univ. Oklahoma, Norman, OK, USA, Tech. Rep., Jun. 2014.

[53] NWS Weather Forecast Office, Norman, OK, USA. (2010). *Information About the May 10, 2010 Tornado Outbreak in Oklahoma*. [Online]. Available: http://www.srh.noaa.gov/oun/?n=events-20100510

Arturo Y. Umeyama (S'16) received the B.S. degree in mechatronics engineering from the National University of Asunción, Asunción, Paraguay, in 2012, and the M.S. degree in electrical and computer engineering from The University of Oklahoma, Norman, OK, USA, in 2016, where he is currently pursuing the Ph.D. degree in electrical and computer engineering.

He is currently a Graduate Research Assistant with the Advanced Radar Research Center, The University of Oklahoma. His research interests include advanced signal processing for weather radars, spectral analysis, and numerical radar simulation.

Sebastián M. Torres (S'98–M'02–SM'07) received the B.S. degree from the National University of Mar del Plata, Mar del Plata, Argentina, and the M.S. and Ph.D. degrees from The University of Oklahoma, Norman, OK, USA, in 1995, 1997, and 2001, respectively, all in electrical engineering.

In 1997, he was with the Cooperative Institute for Mesoscale Meteorological Studies, The University of Oklahoma, where he was the Leader of the Advanced Radar Techniques Group and is currently an Assistant Director and a Senior Research Scientist affiliated with National Severe Storms Laboratory (NSSL). His current research interests include innovative signal processing and adaptive sensing techniques to improve the quality, coverage, accuracy, and timeliness of meteorological products from weather radars, the exploration and demonstration of unique capabilities offered by multifunction phased-array radar for weather observations, and the transfer of technology to existing radar systems in government, public, and private organizations.

Dr. Torres is a member of the Graduate Faculty and the Advanced Radar Research Center, The University of Oklahoma. He has received the 2011 Department of Commence Gold Medal, as a member of the Radar Research and Development Division, NSSL, for scientific and engineering excellence in adapting military phased-array radar technology to improve U.S. weather radar capabilities, and the 2003–2004 Office of Oceanic and Atmospheric Research Outstanding Scientific Paper Award. He was an Adjunct Faculty with the School of Electrical and Computer Engineering, The University of Oklahoma.

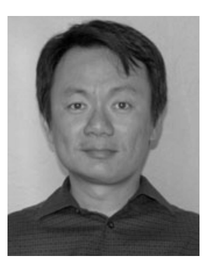

Boon Leng Cheong received the Ph.D. degree in electrical engineering from the University of Nebraska-Lincoln, Lincoln, NE, USA, in 2005, with a dissertation on Adaptive Beamforming to Observe the Atmospheric Boundary Layer Using the Turbulent Eddy Profiler.

He is currently a Research Scientist with the Advanced Radar Research Center and an Adjunct Assistant Professor with the School of Electrical and Computer Engineering, The University of Oklahoma, Norman, OK, USA. His research interests include software-defined radar design, array signal processing, real-time software architecture, parallel computing, and numerical radar simulation.